AGU PUBLICATIONS

JGR

Journal of Geophysical Research: Solid Earth

RESEARCH ARTICLE
10.1002/2017JB014448

Special Section:
Slow Slip Phenomena and Plate Boundary Processes

A geodetic matched filter search for slow slip with application to the Mexico subduction zone

B. Rousset[1], M. Campillo[2], C. Lasserre[2], W. B. Frank[3], N. Cotte[2], A. Walpersdorf[2], A. Socquet[2], and V. Kostoglodov[4]

[1]Department of Earth and Planetary Sciences, University of California, Berkeley, California, USA, [2]ISTerre, Université Grenoble Alpes, CNRS, IRD, Grenoble, France, [3]Department of Earth, Atmospheric, and Planetary Sciences, Massachusetts Institute of Technology, Cambridge, Massachusetts, USA, [4]Instituto de Geofísica, Universidad Nacional Autónoma de México, Coyoacan, México

Key Points:
- We developed a geodetic matched filter that specifically allows for the search of low-amplitude slow slip events
- Synthetic tests show that this method is able to resolve $M_w > 6$ events in the context of the Mexico subduction zone
- The application on real data between 2005 and 2014 enables to detect 28 slow slip events of M_w between 6.3 and 7.2 in the Guerrero area

Supporting Information:
- Supporting Information S1
- Table S1

Correspondence to:
B. Rousset,
rousset@berkeley.edu

Citation:
Rousset, B., M. Campillo, C. Lasserre, W. B. Frank, N. Cotte, A. Walpersdorf, A. Socquet, and V. Kostoglodov (2017), A geodetic matched filter search for slow slip with application to the Mexico subduction zone, *J. Geophys. Res. Solid Earth*, *122*, doi:10.1002/2017JB014448.

Received 16 MAY 2017
Accepted 17 AUG 2017
Accepted article online 23 AUG 2017

Abstract Since the discovery of slow slip events, many methods have been successfully applied to model obvious transient events in geodetic time series, such as the widely used network strain filter. Independent seismological observations of tremors or low-frequency earthquakes and repeating earthquakes provide evidence of low-amplitude slow deformation but do not always coincide with clear occurrences of transient signals in geodetic time series. Here we aim to extract the signal corresponding to slow slips hidden in the noise of GPS time series, without using information from independent data sets. We first build a library of synthetic slow slip event templates by assembling a source function with Green's functions for a discretized fault. We then correlate the templates with postprocessed GPS time series. Once the events have been detected in time, we estimate their duration T and magnitude M_w by modeling a weighted stack of GPS time series. An analysis of synthetic time series shows that this method is able to resolve the correct timing, location, T, and M_w of events larger than M_w 6 in the context of the Mexico subduction zone. Applied on a real data set of 29 GPS time series in the Guerrero area from 2005 to 2014, this technique allows us to detect 28 transient events from M_w 6.3 to 7.2 with durations that range from 3 to 39 days. These events have a dominant recurrence time of 40 days and are mainly located at the downdip edges of the $M_w > 7.5$ slow slip events.

1. Introduction

Deformation related to plate tectonics is mainly accommodated by slip on plate interfaces that can generate measurable seismic waves in the case of earthquakes or can be aseismic if the slip is so slow that the waves are not perceptible. The fault behavior during the interseismic period is usually characterized by the interseismic coupling ratio, typically measured geodetically and defined as the ratio of the slip deficit rate and the long-term tectonic loading rate. This coupling ratio represents an average value in space, due in particular to limitations in data sampling and model assumptions. It is also, most often, averaged in time over the study period, as detecting nonlinear, temporal variations of aseismic slip during the interseismic period remains a methodological challenge. A partially coupled area is thus considered to be spatially homogeneous and aseismically slipping at a steady rate. However, numerous observations highlight the existence of transient aseismic slip events or slow slip events (SSEs) with a wide spectrum of spatial and temporal behavior [e.g., *Obara and Kato*, 2016], sometimes with amplitudes below the noise level of present-day observations [*Frank*, 2016].

Many techniques have been developed to characterize transient aseismic slip on faults since their discovery in the late 1990s [*Linde et al.*, 1996; *Dragert et al.*, 2001]. Most of the observations have been made with data analysis of continuous Global Positioning System (GPS) time series. The number of stations in operation has tremendously increased in the last decades, reaching more than 1000 stations in the Western U.S. or in Japan, improving considerably the ability to detect transient signals and the modeling of associated slip. Some transient slips have recently been detected with Interferometry Synthetic Aperture Radar (InSAR) measurements along strike-slip faults [e.g., *Wei et al.*, 2009; *Shirzaei and Bürgmann*, 2013; *Jolivet et al.*, 2013; *Rousset et al.*, 2016a] and subduction zones [*Cavalié et al.*, 2013]. However, the amount of atmospheric noise and the limited time resolution lead to detection thresholds in magnitude still higher than those obtained with dense GPS networks.

The displacement time series recorded by GPS stations are a sum of various components that may be separated in order to extract transient slip events. *Segall and Matthews* [1997] proposed a network inversion filter of GPS time series, where the displacement is a combination of a secular velocity, slip on faults, benchmark motions, reference frame errors, and estimation errors. The stochastic description of all these parameters is explored through a Kalman filter in time. Many studies have used this formalism [e.g., *McGuire and Segall*, 2003; *Miyazaki et al.*, 2003; *Bartlow et al.*, 2011], sometimes adding complexities to the model, such as *Ohtani et al.* [2010], who decomposed the signal in the wavelet domain.

Others techniques do not assume physical processes to model the GPS time series. *Ji and Herring* [2013] first smooth the time series in time with a Kalman filter to increase the signal to noise ratio. They then detect transient signals through a first-order Gauss-Markov process before applying a spatial principal component analysis to characterize the spatial shape of the detected events. *Riel et al.* [2014] decompose time series with a dictionary of all possible orthogonal functions that could represent the signal, using B-splines to model transient signals. The analysis of the resulting coefficients for each function at each time allows for the detection of individual events. A spatial weighting is applied to take into account the non-homogeneous distribution of stations and filters nearby coherent signals. The approach of *Walwer et al.* [2016] differs from the previous ones in the functions used to decompose the signal. Instead of using harmonic functions which do not allow for interannual variability, this study uses a spectral analysis to retrieve empirical basis functions that represent the common modes and the temporal variability of any data set. Not relying on physical processes, these three methods can be used to detect any transient geophysical process, such as hydrological loading, volcanic magma motion, or slow slip events.

All these methods seem to be efficient in modeling transient signals emergent from the noise automatically. But the detection of transient signals with amplitude close to that of the background noise or even below is more uncertain. This might be due in part to the temporal smoothing which is often applied and to the detection thresholds, set by the amplitude of noise as all time series are modeled separately, even if the spatial covariance is taken into account. However, transient signals with amplitude close to the background noise or lower are likely to occur. For example, in subduction zones, many tremors or low-frequency earthquakes (LFEs) are detected with no corresponding transient signals directly observed in GPS time series [e.g., *Brown et al.*, 2013; *Frank et al.*, 2015; *Obara and Kato*, 2016]. One way to determine if aseismic slip is associated with these seismic events of very low amplitude is to use these events as a monitor of transient slip. In the Mexico subduction zone, *Frank et al.* [2015] use the timing of LFEs bursts to select short windows around these times from the GPS time series and stack them to increase the signal to noise ratio. They successfully extracted a slow slip-like signal corresponding to the average surface motion of all stacked events.

However, by stacking different events in time, the underlying assumption is that these events are exact repeats, which prevents characterization of possible spatiotemporal differences between events. It would then be more convenient to detect transient events independently and solely from GPS time series. *Nishimura et al.* [2013] and *Nishimura* [2014] developed a method to detect short-term SSEs coincident with the tremor activity in Japan, that were previously observed only with tiltmeters. The SSEs detection is made using the Akaike information criterion, to decide whether windows of filtered GPS time series are best fitted with a linear fit alone or with a linear fit plus a step. With this method, they found more than 200 probable M_w 5.6 to 6.8 SSEs along the Nankai trough and the Ryukyu Trench in a 17 year period from 1996 to 2013.

In the present paper, we propose an alternative to Nishimura's method, which, in particular, does not characterize the duration of the events. Our approach is based on a GPS-matched filter, with a physical model of slow slip incorporated in the detection process. We build templates of surface displacement time series from synthetic slow slip that we correlate with postprocessed GPS time series. The correlation is made on ground velocity time series, inspired by the matched filter developed for seismograms to detect low-magnitude seismic events [*Gibbons and Ringdal*, 2006]. Once an event is detected in time, we perform further analyses to best describe its location, duration, and magnitude. In section 2, we first present the formalism of the technique, and we apply it to synthetic GPS time series to assess the detection capability of the method and explore its limits in estimating duration and magnitude of small SSEs. In section 3, we apply it to the Guerrero segment of the Mexico subduction zone where large $M_w \sim 7.5$ SSEs are recurrent [*Radiguet et al.*, 2012; *Graham et al.*, 2016; *Radiguet et al.*, 2016] and the occurrence of smaller ones have been reported [*Vergnolle et al.*, 2010; *Frank et al.*, 2015; *Frank*, 2016]. This area is particularly favorable for such an application as (1) a relatively dense GPS network has produced high-quality time series since 2005 [e.g., *Walpersdorf et al.*, 2011], (2) the flat slab

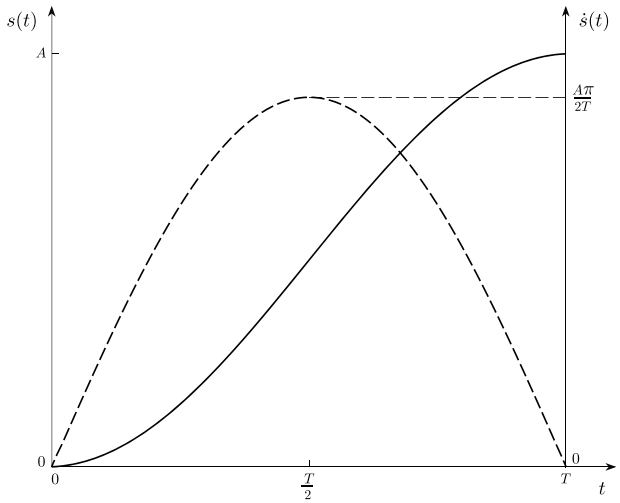

Figure 1. Temporal evolution of the template slip and its derivative. The solid line $s(t)$ represents the slip time evolution used in templates with a slip acceleration from 0 to $T/2$ and a slip deceleration from $T/2$ to T. The maximum slip amplitude is A. Its derivative $\dot{s}(t)$ represented in dashed line is a positive lobe with a maximum at $T/2$.

geometry of the subduction at ~40 km depth just below the continental crust [*Kim et al.*, 2010] allows for the detection of low-magnitude events compared to other subduction zones, and (3) independent catalogs of tremors [*Husker et al.*, 2012] and LFEs [*Frank et al.*, 2014] have already been produced during the period of the MASE (Meso-America Subduction Experiment) seismic network deployment from 2005 to 2007 [*Caltech*, 2007], allowing for a comparison with our detections for this period. Finally, in section 4 we discuss the efficacy of our method, the mechanical characteristics of the detected events and their scaling laws.

2. Formulation of the Geodetic Matched Filter

2.1. Templates of Surface Displacement Time Series

The physical model that we use to detect transient slip events is based on the classical static Green's functions that link slip on a given area of a subduction interface to static surface displacement at each GPS station $\mathbf{w}^i_s$, where i corresponds to the north and east components and s stands for the finite static displacement. In this study, we compute the Green's functions using the discrete wave number method [*Bouchon*, 1981, 2003] in an elastic stratified medium, assuming the *Hernandez et al.* [2001] velocity model and using the AXITRA software [*Coutant*, 1989]. The subduction interface consists of two planes, as used by *Radiguet et al.* [2012] and *Rousset et al.* [2016b]. One initiates at the trench, dipping 15° to the northeast, and connects to the other, horizontal one continuing inland beneath the continent. Each plane is made of 10 patches along dip by 60 patches along strike. Each patch measures 13.4 km in dip direction and 13 km in strike direction. The temporal slip evolution for a slip of unit amplitude is given by the function

$$s(t_1) = \frac{1}{2}\left[1 - \cos\left(\frac{\pi t_1}{T}\right)\right] \tag{1}$$

where t_1 is the time vector of the template and T is its total duration (Figure 1). The temporal sampling of t_1, Δt, is a daily sampling for the GPS time series used in this study. $s(t)$ is symmetrical, with half of its duration corresponding to slip acceleration, followed by a deceleration during the second half duration, which is a reasonable evolution for the short-term slow slips we are searching for. For these low-amplitude events, we do not consider any spatial propagation. $s(t)$ also has the advantage to have an easily obtained analytical derivative

$$\dot{s}(t_1) = \frac{\pi}{2T}\sin\left(\frac{\pi t_1}{T}\right) \tag{2}$$

The template displacement time series at each GPS station are thus given by

$$\mathbf{w}^i(t_1) = \mathbf{w}^i_s s(t_1) \tag{3}$$

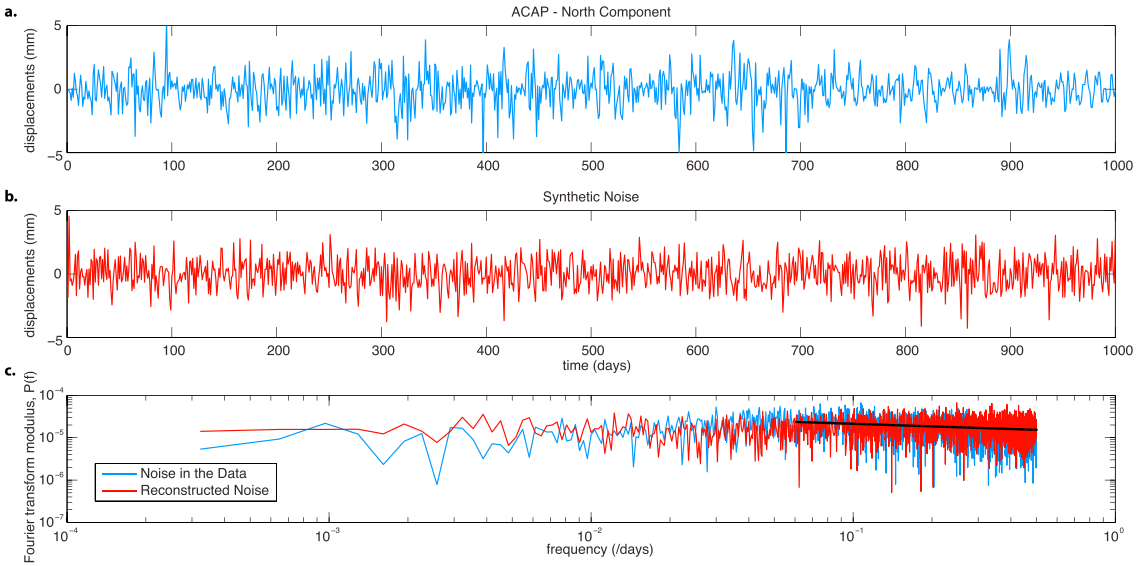

Figure 2. Synthetic time series of noise. (a) The 1000 days of the postprocessed time series at station ACAP in Mexico for the northern component. Long-term SSEs and earthquakes have been removed. We can see the daily scatter and longer period transients. (b) The 1000 days of reconstructed time series of noise at the same station. (c) Fourier transform modulus $P(f)$ of the real ACAP times series in blue and the reconstructed one in red. The black line denotes the slope used to model the colored noise (spectral index $n = 0.42$ in that example).

2.2. Continuous Correlation of Templates and GPS Time Series

We compute the correlation function $\mathbf{C}^i(t)$ between the template time series $\mathbf{w}^i(t_1)$ and the GPS time series $\mathbf{d}^i(t)$ recorded for the i north and east components at each station, t being the discrete time vector of the full time series. In this section, $\mathbf{d}^i(t)$ are synthetic time series to explore the detection capabilities of the method. These synthetics are constructed as a sum of GPS realistic noise and transient events due to slow slip on the modeled subduction interface. A power law model $P(f) = P_0/f^n$, where f is the frequency, n is the spectral index, and P_0 is a normalizing constant, is used to describe the GPS time series noise. *Williams et al.* [2004] show that GPS noise is best modeled with a sum of white noise, for which $n = 0$, and colored noise, for which $n > 0$, $n = 1$ corresponding to a flicker noise process and $n = 2$ to a random walk process. To model noise for the time series of the Mexican GPS network, we fit the spectrum of cleaned GPS time series (time series processing is explained in section 3) with power laws to explain both white and colored noise at each station (Figure 2).

Time windows of $\mathbf{d}^i(t)$ with the same norm as $\mathbf{w}^i(t_1)$ are defined on $t_2 = (t - t_1/2, \dots, t + t_1/2)$ with the same temporal sampling as t_1, Δt, so that $||t_1|| = ||t_2|| = N$, N being the number of days of the template. The inner product between $\mathbf{w}^i(t_1)$ and $\mathbf{d}^i(t_2)$ is defined by

$$\left\langle \mathbf{w}^i(t_1), \mathbf{d}^i(t_2) \right\rangle_{N,\Delta t} = \sum_{j=0}^{N-1} w^i(t_1 + j\Delta t) d^i(t_2 + j\Delta t) \tag{4}$$

In order to optimize the correlation operation, it is preferable to correlate non-monotonic functions. The discriminatory nature of the stationary point of the surface velocity (time derivative of the surface displacement) during the middle of a slow slip event improves the timing precision of our detection. We thus use the temporal derivatives of $\mathbf{w}^i(t_1)$ and $\mathbf{d}^i(t)$. The fully normalized correlation function is defined as

$$\mathbf{C}^i(t) = \frac{\left\langle \dot{\mathbf{w}}^i(t_1), \dot{\mathbf{d}}^i(t_2) \right\rangle_{N,\Delta t}}{\sqrt{\left\langle \dot{\mathbf{w}}^i(t_1), \dot{\mathbf{w}}^i(t_1) \right\rangle_{N,\Delta t} \left\langle \dot{\mathbf{d}}^i(t_2), \dot{\mathbf{d}}^i(t_2) \right\rangle_{N,\Delta t}}} \tag{5}$$

and the weighted correlation $\mathbf{C}_\mathbf{w}$ is

$$\mathbf{C}^i_\mathbf{w}(t) = \frac{|\mathbf{w}^i_s|}{\max\left(|\mathbf{w}^i_s|\right)} \mathbf{C}^i(t) \tag{6}$$

The final function on which we test the detection of transient events is the sum of the weighted correlation functions over all stations and both horizontal components. We select only the stations for which

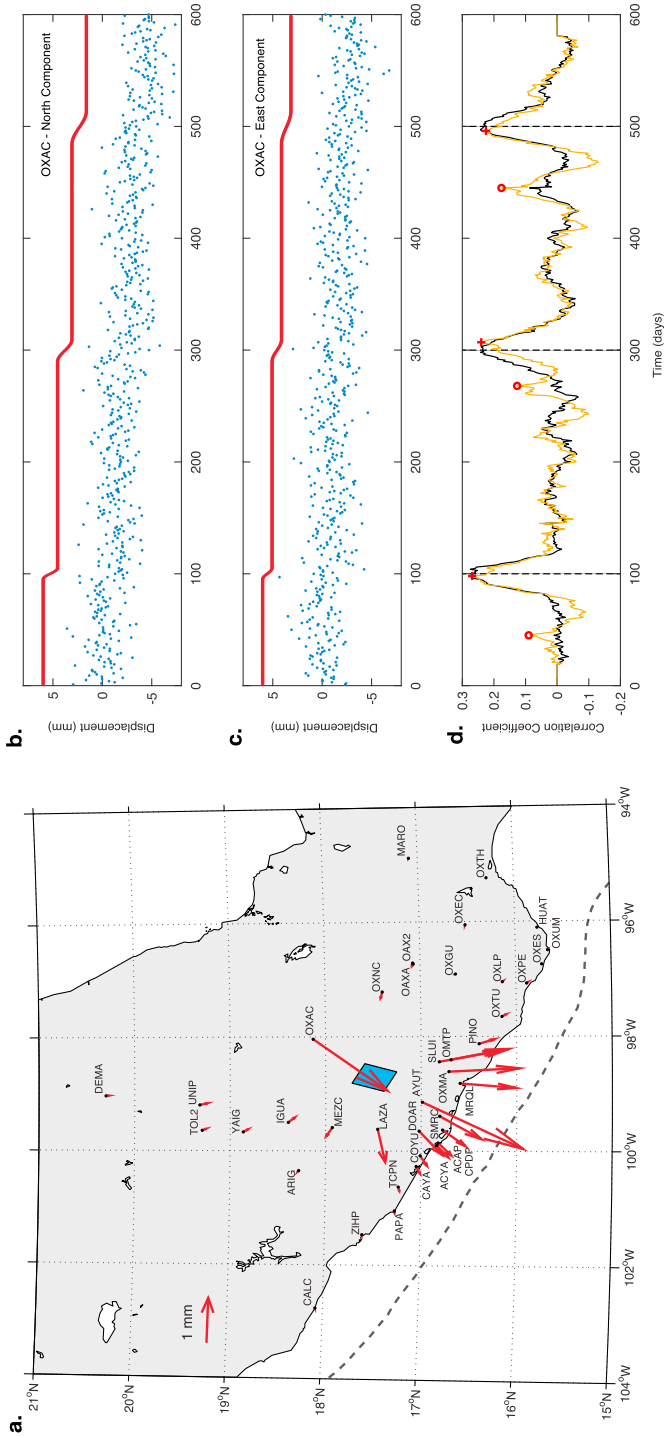

Figure 3. Example of correlation analysis for a M_w 6.1 synthetic slow slip event. (a) The blue area (corresponding to nine patches) is sliding with a slip of 0.05 m. The static surface displacement due to this slow slip is shown by the red arrows. OXAC and AYUT are the stations with the maximum amplitude of surface displacement, of ~2 mm. (b) Synthetic time series at station OXAC, for the north component. The bold red curve shows three transient events (a 10 day transient event centered on time 100 days, a 20 day transient event centered on time 300 days, and a 30 day transient event centered on time 500 days). The blue dots show the synthetic time series built from these three transient events plus noise. The transient events are almost impossible to detect by visual inspection, having an amplitude 2 times lower than the noise amplitude. (c) Same as Figure 3b but for the east component. (d) The yellow (respectively black) curve shows the sum of the unweighted (respectively weighted) correlation functions of all stations and both horizontal components. The template used for the correlation has a duration of 30 days. Red crosses at highest correlation peaks identify detections of the synthetic slow slip events, while red circles show secondary peaks of correlation corresponding to the noise, which are both further analyzed in Figure 4. The black curve shows the sum of the weighted correlation functions. Note that while amplitudes are identical at synthetic events of the weighted and unweighted correlation functions (red crosses), amplitudes are reduced at noise peaks in the weighted correlation function (red circles). Dashed black lines indicate times of transient slip events.

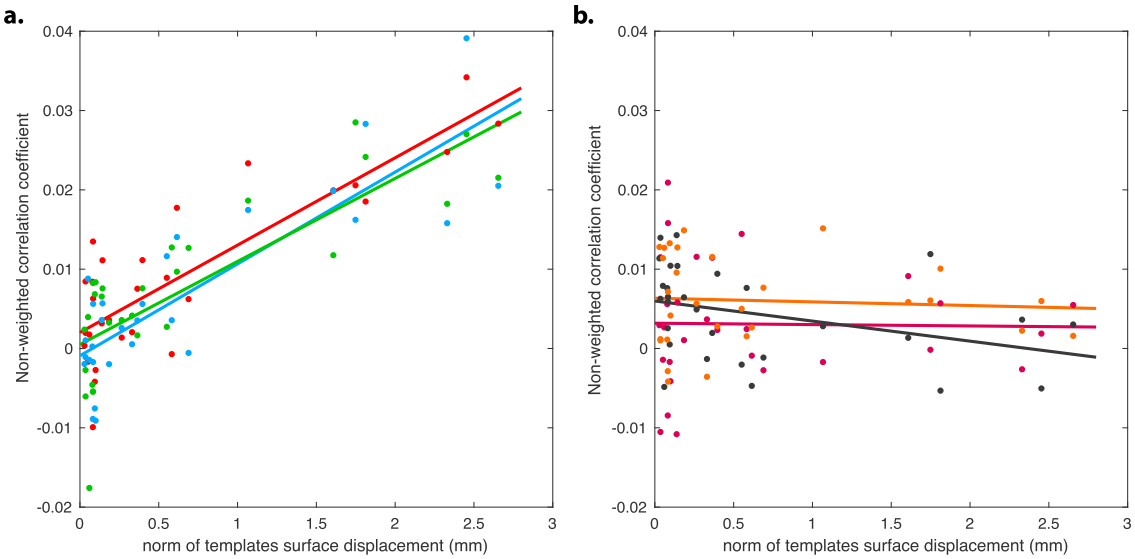

Figure 4. Correlation coefficient as a function of the norm of the surface templates displacements for the non-weighted correlation function. (a) Relation for the red crosses in Figure 3d. Dots correspond to the correlation coefficient obtained at each station and bold lines are the linear fits. Red is for the event detected at time 97, blue for the event at time 300, and green for the event at time 497. (b) Same as Figure 4a but for the red circles in Figure 3d. Burgundy is for the noise peak at time 45, black for the noise peak at time 268, and orange for the noise peak at time 445.

$w_s^i > \alpha \times \max(\mathbf{w}_s^i)$, α being an empirical coefficient that we set to 0.1 in this section. This selection enables us to discard from the summation of stations those recorded nonexistent or too small amplitude transient signals.

Figure 3 presents an example of a correlation analysis for a synthetic slow slip event of M_w 6.1 located in the central part of the flat slab of the Mexico subduction zone (Figure 3a). At stations that recorded the highest displacement for this event, such as OXAC, the displacement is ~2 mm, which is 2 times less than the amplitude of the background noise (Figures 3b and 3c). However, the sum of all non-weighted or weighted correlation functions over the whole network shows peaks emerging at times of the transient events (red crosses, Figure 3d). Secondary, lower high amplitude peaks are also present at times corresponding to pure noise, but only when non-weighted correlation functions are used (red circles, Figure 3d). The use of weighted correlation functions is thus a way to better discriminate between transients slip events and noise. The correlation coefficient for the non-weighted correlation function, represented as a function of the norm of the surface template displacement for all peaks corresponding to transient events, shows that higher surface template displacements produce higher correlations for transient slip events (Figure 4a). This observation is not necessarily obvious when reasoning only in terms of correlation, as different amplitude transients recorded at a given network of stations, should give identical correlation amplitudes. However, due to the presence of noise, which has similar amplitudes at all stations, the signal-to-noise ratio is larger at stations that record the highest transient amplitudes, producing higher correlation amplitudes. On the contrary, at peaks recorded at times without transient slip events, we can see from the non-weighted correlation function that the noise is spatially randomly distributed, with coefficients between −0.02 and 0.02 (Figure 4b). In other terms, the slopes in Figure 4 are always highly positive for transient slip events and close to zero for the noise. To take advantage of this spatial discrepancy between slow slip patterns and noise patterns in the correlation function, we weight the sum of each station correlation functions to attribute more weight to stations that have a template surface displacement of higher amplitude (equation (6)). The benefits of this weighting are clear on Figure 3d, where weighted and non-weighted correlation functions have identical peak amplitudes at times of slow slip transients, while the amplitude of noise peaks is reduced in the weighted correlation function.

Detections of transient events thus correspond to the maximum amplitude peaks of the weighted correlation function. For a given location, the only parameter of the template that influences the amplitude of the correlation is its duration. Figure 5a shows that for synthetic time series without noise the right template duration gives a correlation of 1, while templates with a duration deviating by plus or minus 10 days from the correct one also give a correlation very close to 1. When noise is taken into account (Figure 5b), the highest

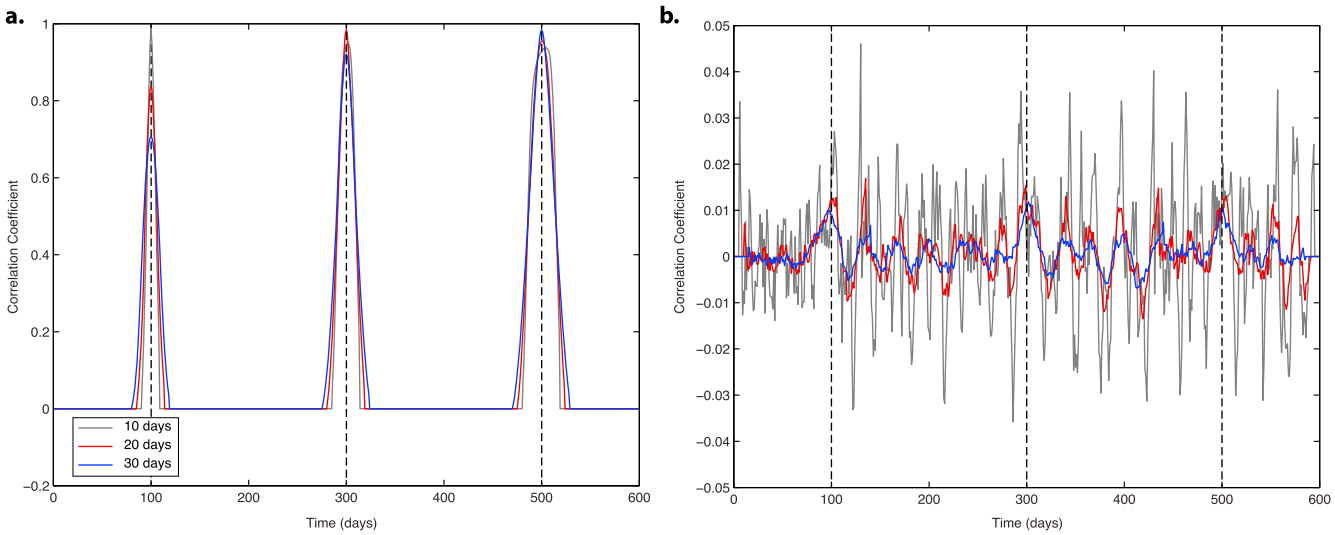

Figure 5. Influence of the template duration on the amplitude of the weighted correlation. (a) Sum of the correlation functions for synthetic time series without noise. The grey curve is for a 10 day template, the red one for a 20 day template, and the blue one for a 30 day template. The synthetic events are the same as in Figure 3. (b) Same as Figure 5a but for synthetic time series with noise. Note that while the amplitude is decreasing for longer templates, the transient slip events are emerging from noise only for the 30 days template. Dashed black lines indicate times of transient slip events.

amplitudes of the correlation are always for the shorter templates because the oscillations in the noise are dominated by the short-term daily white noise oscillations. However, transient events emerge from the noise in the final correlation function for templates longer than 30 days. In the blue curve of Figure 5b (which is the same as the black curve of Figure 3d), the amplitude of the correlation at times of transient events is at least twice higher than the amplitude at only noise times. We conclude from these tests that only templates with durations longer than 30 days can be used to discriminate correlation peaks due to transient slip from those due to noise. Finally, for a given detection in time, we attribute the location of the slip to the patch on the subduction interface that maximizes the weighted correlation (see the statistical analysis of the slip location in section 2.4).

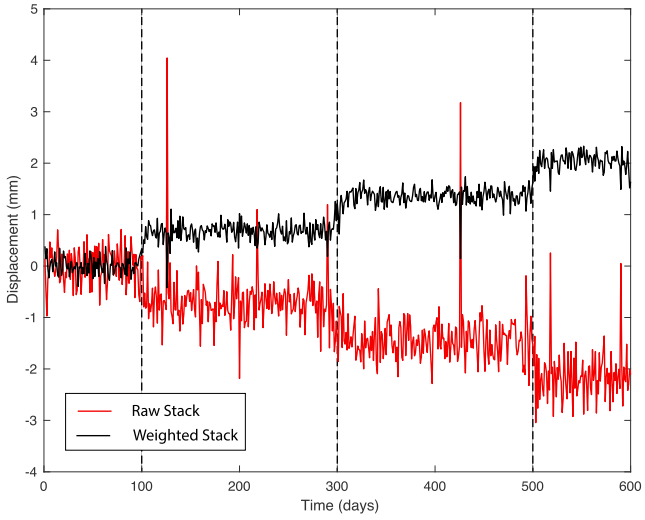

Figure 6. Stack of GPS displacement time series. The raw stack of all GPS time series, for north and east components, is in red. In black, the stack is weighted by the amplitudes and polarities of the surface displacements of the template. Note that the signal-to-noise ratio is increased by a factor of 3 in the weighted stack. Dashed black lines indicate times of synthetic transient slip events.

2.3. Duration and Magnitude Estimation

Once an event is detected and located, our aim is to estimate its duration and magnitude. As the correlation function is computed using velocity time series (equations (5) and (6)), we lose the amplitude information that corresponds to the magnitude of the event. We consequently have to examine the GPS displacement time series directly. As transient signals on individual time series might be so small compared to the noise that it becomes impossible to characterize them, we stack the time series over the network (Figure 6). To give more weight to stations that recorded the highest amplitude signal, we apply the same weighting for the stack as for the correlation function (equation (6)). This weighting has the advantage to give to each weight the right sign, which is not the case for a raw stack. In the Mexico subduction

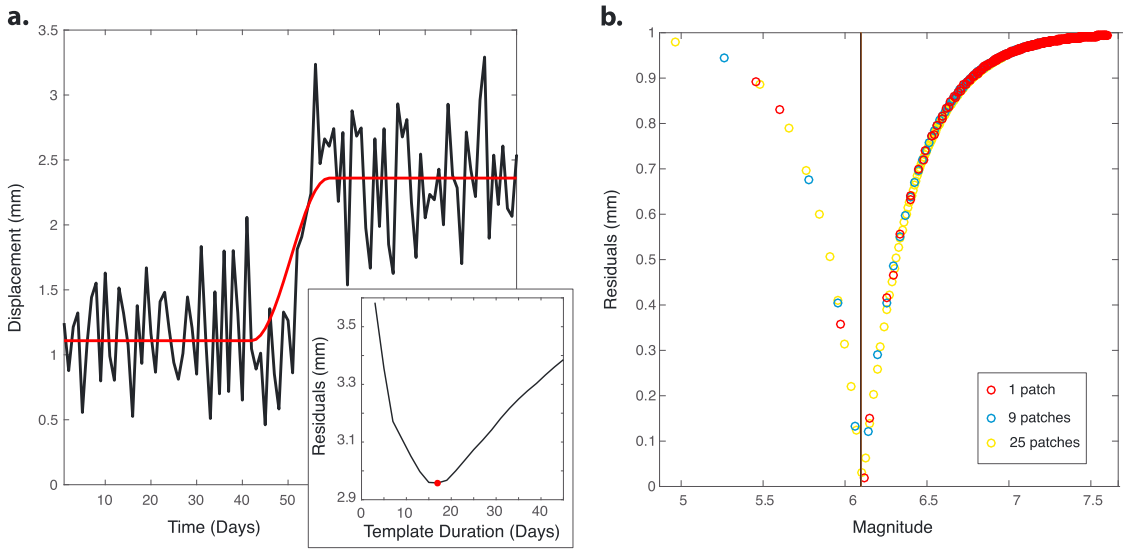

Figure 7. Estimation of the duration and magnitude of a synthetic transient event. (a) The black curve shows a 100 day window of the weighted GPS displacement stack. The red curve presents the best model. In inset, the residuals for models with variable transient durations show that the best fit is for a 17 day transient, while the true duration is 20 days. (b) Residuals between the estimated step of the transient in Figure 7a and the steps obtained from synthetic events of different magnitudes, obtained by exploring the source slip area and slip amplitude parameters. Each circle corresponds to a different slip value ranging from 1 mm to 1 m equally spaced by 5 mm. The red, blue, and yellow circles represent the three slip areas tested, 1 patch, 9 patches, and 25 patches, respectively, always centered on the location of the event. The vertical line indicates the true magnitude.

zone, surface displacements due to slow slip events are mainly recorded in the north component, so that on stations located to the east and west of a sliding patch, the east components have opposite signs. Simply stacking these opposite signs would wipe out the signal. As we can see in Figure 6, the weighted stack has a much better signal to noise ratio than the raw stack.

In order to estimate the duration and the magnitude of a detected event, we model the weighted stack of GPS displacements. On a time window centered on the detection time, the model includes a transient signal modeled by $s(t)$ and linear terms before and after the transient. For the synthetic tests, we fix the length of the window to 100 days, knowing that the transients events are shorter than 30 days. The best model is then estimated in a least squares sense, with more weight at the center of the window. To compute the residuals, the stacks of the displacement time series are weighted by a triangular-shaped function that has an amplitude of one at its center and zero at its edges. We test various models with varying transient durations and the preferred duration corresponds to the model that minimizes the residuals (Figure 7a).

Finally, once the duration has been estimated, we measure the amplitude of the displacement in the weighted stack during the transient event. To estimate the magnitude, we compare this amplitude to amplitudes obtained with templates of varying source slip area and slip amplitude. Given the small size of the events, several combinations of slip area and slip amplitude equally fit the step amplitude in the stack (Figure 7b). This means that we can only retrieve information about the magnitude of the events, without being able to extract more details about the source properties.

2.4. Statistics on Synthetics

To discuss the resolution and limitations of our GPS matched filter, we first compute 1000 iterations of noise by station. Then, we construct synthetic time series at GPS stations, as combinations of each iteration of noise with synthetic transients of various times, locations, durations, and magnitudes. Seventy locations of transients are tested (regularly spaced on the subduction interface, Figure 9), with durations of 10, 20, or 30 days, and magnitudes between 5.6 and 7 (the slip area is fixed to nine patches and nine values of slip are tested, between 1 cm and 1 m). We then apply the GPS matched filter to these synthetic time series, to first estimate the time of the transients, then their location (for the location estimates, we use 100 synthetic time series by stations instead of 1000 to save computing time), and their duration and magnitude are explored. We compare the estimated parameters of the detected transients to the true parameters. The estimated detection times and durations of the events have Gaussian-like distributions so that we can estimate a mean

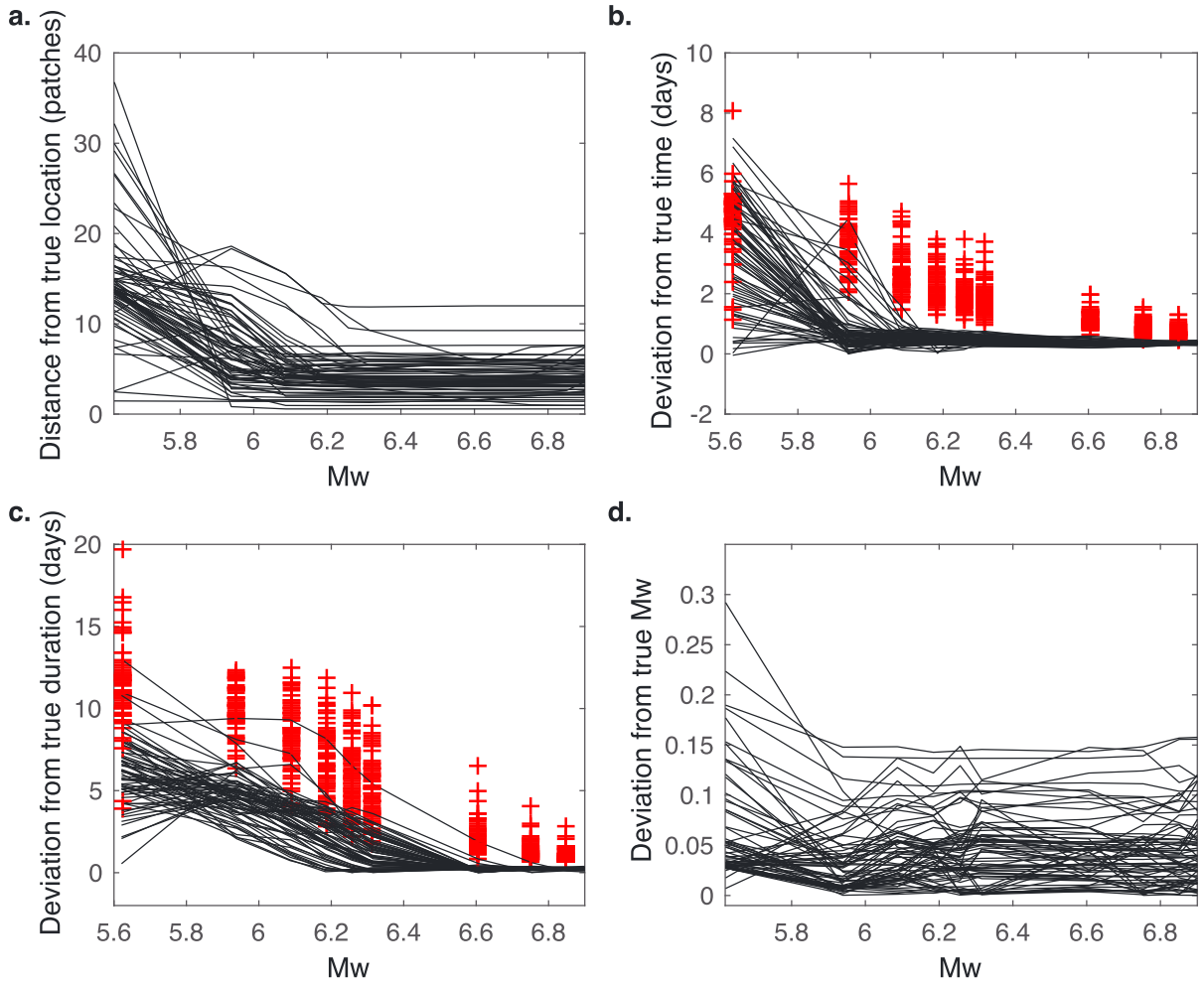

Figure 8. Deviations from true locations, times, durations, and magnitudes as a function of the magnitude. (a) The black curves show the mean of the distance between the estimated location and the true location as a function of the magnitude. These distributions are for 100 noise draws by tested patch (70 patches tested). (b) Same as Figure 8a but for the deviation from true times of the event in absolute value (the mean has been computed on 1000 samples for all parameters except the location). As the distributions of the deviation are Gaussian like, we also estimated the standard deviation for each sample, represented by the red crosses. (c) Same as Figure 8b but for the deviation from the true duration. The true event duration is 20 days in this example. (d) Same as Figure 8a but for the deviation from the true magnitude. The draw has been made on 1000 samples.

and a standard deviation for each distribution. The location and magnitude estimated are similar whatever the noise draw, with narrow distributions. Magnitude distributions might present several, close peaks, corresponding to different tested slip areas. Figure 8 presents the mean of the distributions for the locations, detection times, durations, and magnitude estimates as well as associated standard deviations for detection times and durations, as a function of the magnitude. Figure 9 shows the same parameters but as a function of the location. The location is overall poorly resolved for magnitudes lower than 5.9 but for higher magnitudes, estimated locations are in most cases within seven patches from the true location (Figure 8a). Magnitude 6.1 synthetic events closely surrounded by GPS stations are the best resolved in terms of location, while, as expected, central events far from all stations and some events bellow the coastline are poorly located due to the lack of offshore stations (Figure 9a). Detection times are always within 8 days of the true time (Figure 8b). For most of the locations, the resolution in the detection time is plus or minus 1 day for events of magnitudes between M_w 5.9 and 6.2, and below 1 day for those above M_w 6.2 with very low standard deviations. The duration of the events is the most tricky parameter to retrieve. In Figure 8c, we present an example of a 20 day event for which the right duration is correctly estimated, in most cases, for $M_w > 6.2$, and correctly estimated for those above M_w 6.6. For lower magnitudes, durations are always underestimated. For events of 20 and 30 days of low magnitudes, durations are always underestimated, while for 10 day events the duration is always overestimated, but with no systematic shift. For the detection times and the durations, mean deviations from true

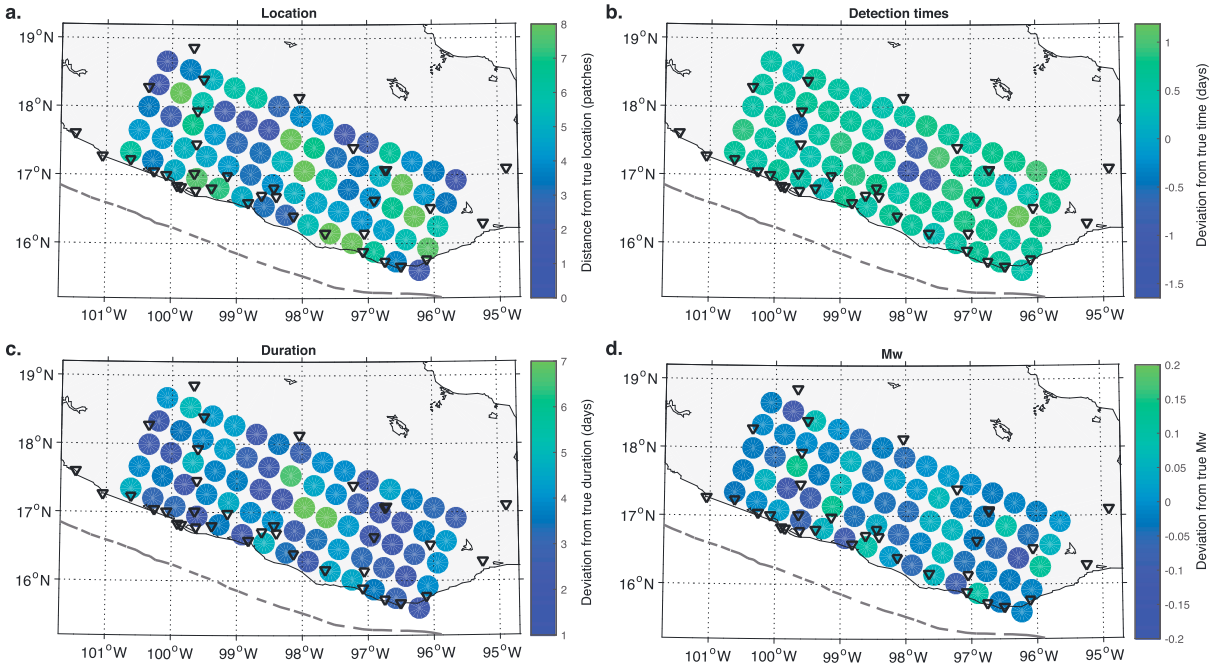

Figure 9. Deviations from true (a) locations, (b) times, (c) durations, and (d) magnitudes as a function of the location. These maps are representing the means computed on 1000 samples (100 for the locations) as in Figure 8. The values represented here correspond to a synthetic transient of equivalent moment magnitude 6.1. Black triangles symbolize the GPS stations. Note that the distance between two colored circles correspond to three patches.

values are rather spatially homogeneous, except for the central events far from all GPS stations (Figures 8b and 8c). Finally, the magnitude is always well retrieved for events larger than M_w 5.6. The means of the deviation between true M_w and estimated M_w are very homogeneous in space (Figure 9d) and are always lower than 0.3, and, in 90% of the cases, lower than 0.1 (Figure 8d).

3. Application to Real Data: The Mexico Subduction Zone Near Guerrero

We apply the previously described methodology to real GPS time series recorded above the Mexico subduction zone, in the area of the Guerrero seismic gap. This area is known to produce the largest amplitude SSEs of the world, with $M_w \sim 7.5$ events [e.g., *Kostoglodov et al.*, 2010; *Radiguet et al.*, 2012; *Graham et al.*, 2016; *Radiguet et al.*, 2016]. We analyzed the period from 2005 to 2014. The beginning of that period, from 2005 to 2007, has the advantage to coincide with independent seismological measurements of tremors [*Husker et al.*, 2012] and LFEs [*Frank et al.*, 2013, 2014] made during the MASE deployment [*Caltech*, 2007]. This will help validate our GPS matched filter approach by analyzing spatiotemporal coincidences and interactions between low-amplitude seismic events and detected slow slip events. We use the data recorded by the 29 GPS stations of the Mexican permanent GPS network in the Guerrero area. The GPS time series have been processed at ISTerre using GAMIT and GLOBK softwares [*Herring et al.*, 2006]. International Global Navigation Satellite Systems service stations from around the world were added to the Mexican network to constrain the reference frame. The International Terrestrial Reference Frame (ITRF) 2008 solution has been used in this study [*Altamimi et al.*, 2011]. We then modeled the time series as a sum of a long-term tectonic linear term, Heaviside functions at times of small earthquakes or antenna manipulations, and decaying logarithm functions, for postseismic signals of significant earthquakes. We then removed the periods of time corresponding to the large 2006, 2009–2010, and 2014 SSEs and corrected for the linear term between those events. The temporal derivative of the resulting time series was then computed for the correlation with the synthetic templates.

We apply the exact same correlation procedure we described for the synthetics tests for the real data. The main difference between the two data sets is that the number of active stations is varying with time for the real data case, leading to a temporal evolution of the detection capability. We apply a minimum threshold of four active stations at the same time to allow for a possible detection. We use a template with a length

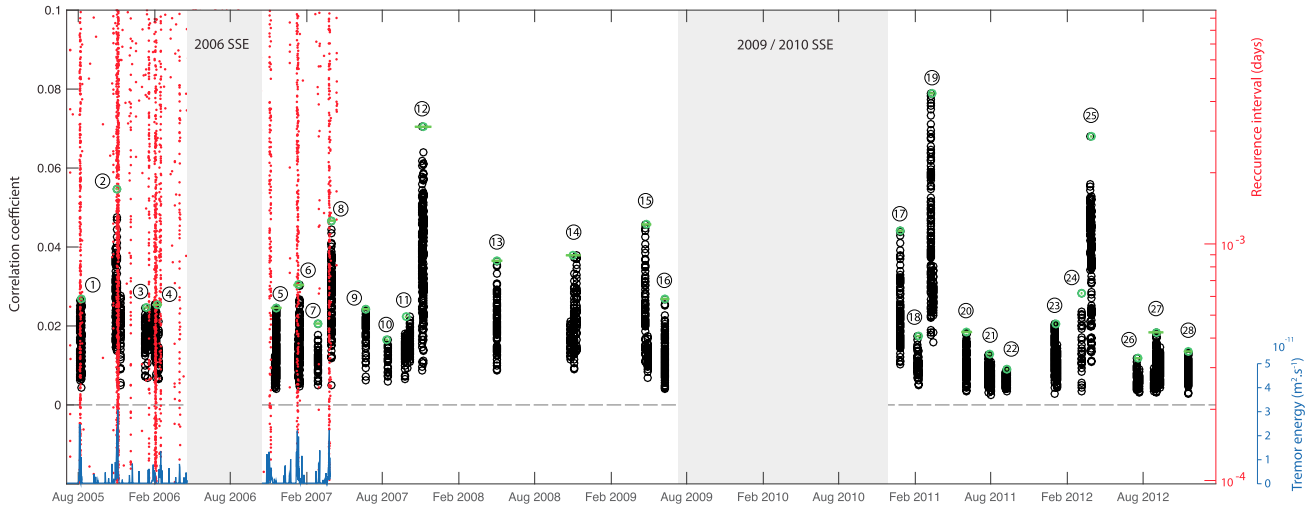

Figure 10. Detections of small slow slip events on the Mexico subduction zone near Guerrero and comparison with tremor and LFEs activities. Black circles show the cleaned detections on all patches. Detections made on less than 30 patches at a given time have been removed. The final detections are shown by green circles, and their estimated durations are indicated by green lines. The blue curve presents the tremor energy [*Husker et al.*, 2012] calculated with a line of seismometers installed from Acapulco to Mexico City from 2005 to 2007 during the MASE [*Caltech*, 2007]. LFEs occurrences detected with the same sensors are shown by red dots [*Frank et al.*, 2014]. We show here only the LFEs that occur in the transient zone. *Frank et al.* [2014] distinguish this updip area with intermittent LFEs from the downdip sweet spot presenting a continuous activity. We cut the recurrence intervals longer than 10^{-2} days in order to select only the closest events in time, representing a dense activity. The 2006 and 2009–2010 SSEs periods not analyzed in this study are shown by grey rectangles.

of 30 days, allowing for searches of events of similar or shorter durations. We validate the detections for peaks of correlation that have an amplitude higher than 15% of the maximum correlation so that even very small events can be detected. As a slip event on a given patch is producing positive detections of lower amplitude on surrounding patches, we keep only the dates for which more than 30 patches have a positive detection. This threshold of 30 patches does not have a strong impact on the number of detections. It instead cleans spurious detections made on a small number of patches.

The resulting detections are clustered (black dots on Figure 10), with several dates closely spaced in time in each cluster. This clustering is due to multiple detections for a given event, corresponding to different locations of the templates for this event. To test if the detections in a cluster correspond to a single event, we estimate the duration of each detected event on the stacked displacement time series. If the estimated durations of two close events intersect, we consider them as a single event. Final detection times (green circles on Figure 10) correspond to the mean of all detections in a cluster of events for which estimated durations intersect. As for synthetics, the location of a detected transient slip corresponds to the patch that presents the maximum correlation at the detection time. We then estimate the duration and magnitude for the detected events. Compared to the duration estimation presented for synthetic data, we make an adaptive estimation in two steps for the real data. The first estimate made on a 30 day sliding window smoothed time series serves as a guide to calibrate the final model window length which is 3 times longer than the first estimate of the duration. Figure 11 presents an example of a detection. The weighted stack of GPS time series is showing a clear transient signal that we modeled to estimate both the magnitude and the duration of the event (Figure 11a). Figures 11b and 11c are showing the individual time series for all GPS stations used in that detection, respectively, for the north and east components. From these individual time series, it is not trivial to identify a transient event. And from the red lines, showing the static displacement at each station once the detection and modeling of the event have been performed, we can see that these displacements have small amplitudes consistent with the data, always below or close to the amplitude of GPS noise level. Note in Figure 11a that the linear slopes in the stack before and after the transient events are not the same. This is an artifact due to the large number of holes in the GPS time series, leading to different number of stations involved in the stack before and after the transient event. The slopes of the stack might be interpreted physically only in case of complete time series. The same figures are presented for all the detected events in the supporting information.

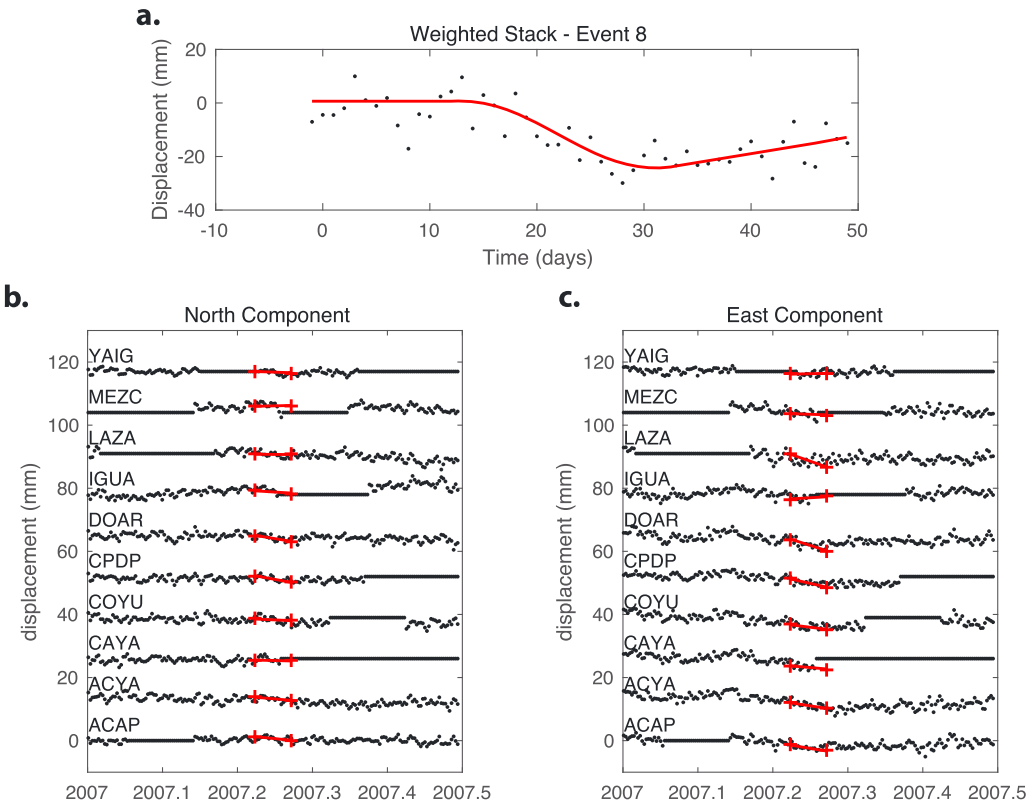

Figure 11. Example of a weighted stack of GPS time series for the Event 8. (a) Stack of the horizontal components of the GPS time series centered on the detection time. The black dots correspond to the data and the red line to the model from which we have estimated the duration and the M_w of the events. (b, c) Independent GPS time series for all the stations used to characterize this event, respectively, for the north and east components. The red lines indicate the static amplitude of displacement at each station based on the location and magnitude estimated. The horizontal black lines highlight periods without measurements. This type of figure is shown for all events detected in the supporting information.

During the MASE observation period, most of the detections seem to coincide in time with high tremor and LFE activity (Figure 10). While some of the detections are shifted compared to the main tremor and LFE activity, like event 5, the duration of the detected SSEs (green lines on Figure 10) always includes the tremor and LFE bursts. Compared to the seven potential SSE dates selected by *Frank et al.* [2015], based on bursts of LFEs in the transient zone, and used to retrieve an average slow slip event with stacked GPS time series, we have independently detected with our analysis, six of the seven events. Only two GPS stations were active at the time of the first burst of LFEs selected by *Frank et al.* [2015], preventing any detection with our procedure. While the average location of the seven events is coincident with the LFE locations in the transient zone [*Frank et al.*, 2015], our locations for events 1 to 8 are at similar depths but spread over larger distances along strike (Figure 12). However, the centroid of the eight events detected corresponds to the average location of *Frank et al.* [2015]. For the complete study period, we have detected 28 transient events, with durations of 3 to 39 days. The recurrence intervals between those events range between 20 and 180 days with a peak of about 40 days (Figure 13). Outliers with recurrence intervals larger than 100 days might be related to missing detections at times when the number of active stations is lower than four. The majority of detected event locations is at the downdip limit of the large SSEs, spread over the length of the large SSEs (Figure 12). Except for two of them, they are all located in areas of low SSE slip (<0.1 m). The events 21 and 25 occur at the western limit of the Guerrero gap, at the transition between a low interseismic coupling area (the gap) and a high coupling area [*Rousset et al.*, 2016b], and are shallower than the other detections. They also occur at the initiation point of the 2014 SSE (Figure 12), where anomalously large slip amplitudes were reported and also at the edge of the Papanoa rupture [*Radiguet et al.*, 2016]. Overall, no clear propagation is observed between the events,

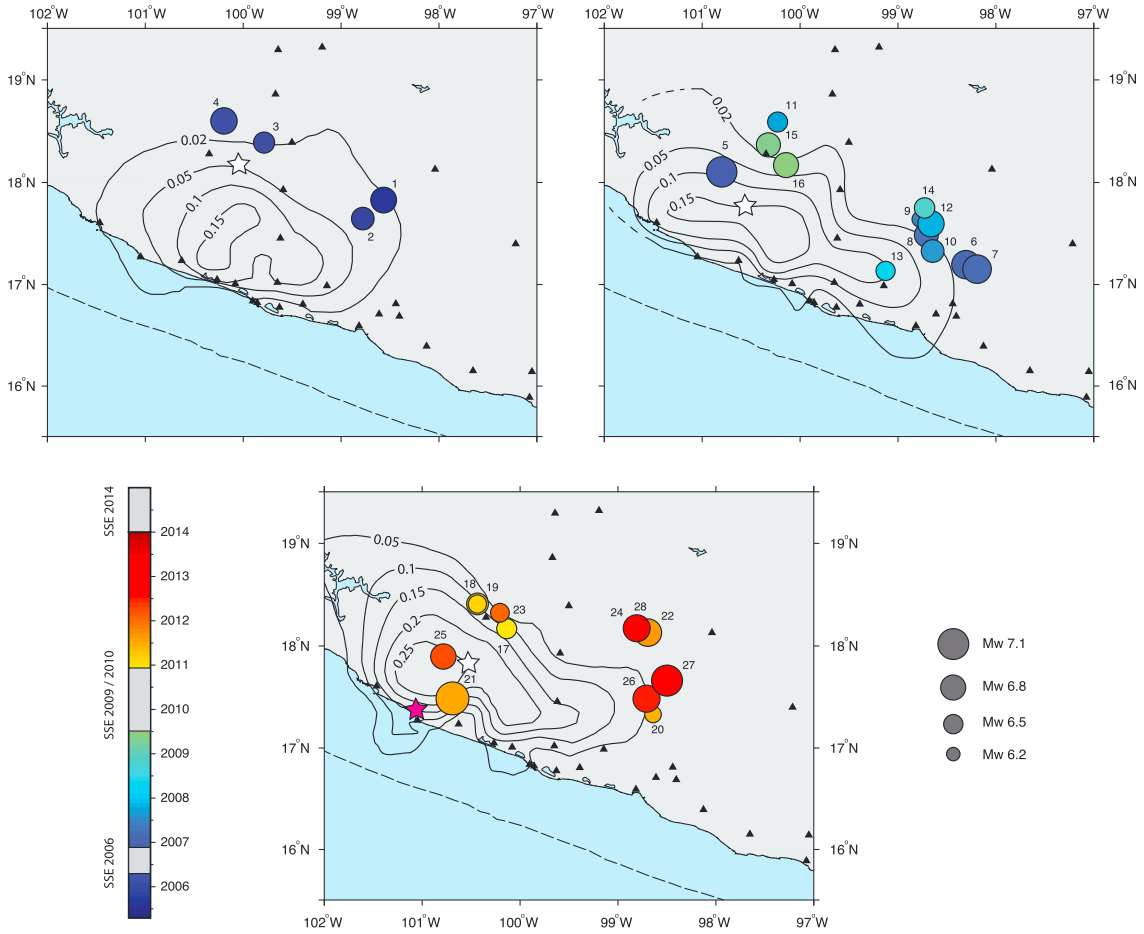

Figure 12. Location of the detected events compared to the slip areas of the 2006, 2009–2010, and 2014 slow slip events. The circles show the locations of the detected events, color coded by their detection times and scaled by their magnitude. The three maps correspond to the periods of time (top left) before the 2006 event,(top right) between the 2006 and the 2009–2010 events, and (bottom) between the 2009–2010 and the 2014 events. The 2006 and 2009/2010 SSEs slip surfaces are depicted by contours of final slip amplitude 0.02, 0.05, 0.1, and 0.15 m, from *Radiguet et al.* [2012]. The 2014 SSE slip surface is shown by contours of final slip amplitude 0.05, 0.1, 0.15, 0.2, and 0.25 m, from *Radiguet et al.* [2016]. The white stars show the initiation of these three SSEs. The purple star indicates the epicenter of the 18 April, M_w 7.3 Papanoa earthquake *Radiguet et al.* [2016]. The time periods of the three large SSEs are indicated in the color scale. GPS stations used are shown by the black triangles. The grey dashed line indicates the location of the trench.

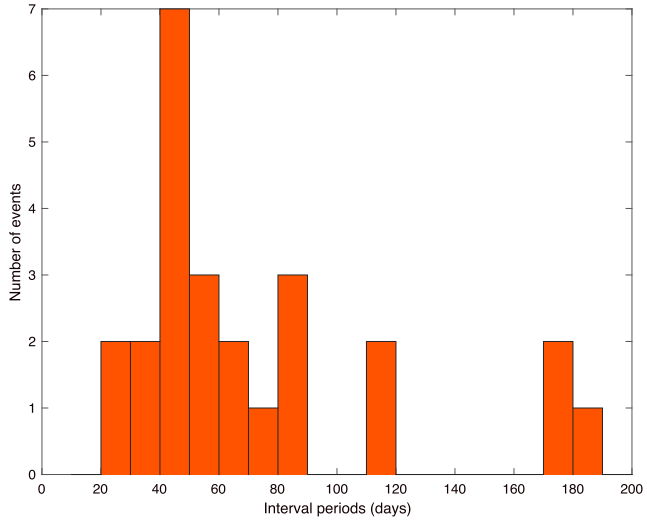

Figure 13. Recurrence intervals between consecutive events detected. Note that we are probably missing events in this study, due to gaps of recording at some GPS stations, which might explain the largest outlier values.

and they seem to occur randomly along strike. We note that some slow slip events preceding the 2006, 2009, and 2014 SSEs are located close to the initiation points of these ruptures. Also, a notable spatial cluster of five events (events 8, 9, 10, 12, and 14), located at the eastern limit of the Guerrero SSEs, occurred around 2008.

4. Discussion

4.1. Discriminating SSEs From Other Phenomena

Using synthetic time series, we have shown that the geodetic matched filter that we developed is able to accurately detect $M_w > 6$ events in the Mexico subduction zone. The application to real data in the Guerrero area detects 28 transient events during the period 2005–2014, in between the large 2006, 2009–2010, and 2014 SSEs. The question about whether or not our method detects transients that do not correspond to slip on the subduction interface is of primary importance. Indeed, located in an area where precipitation is important, GPS stations are expected to record seasonal oscillations due to ground loading variations, as well as more local effects such as aquifer extraction and recharge. Contrary to other methods that try to separate all components that have similar temporal covariances over the network [e.g., *Walwer et al.*, 2016], the method developed here aims at extracting only transient slips based on a physical model. As the correlations are made on both east and north components, the scale and the pattern of the template surface displacements will discriminate detections of slow slips from possible detections of other physical processes. For example, a large-scale common mode motion of the GPS network will produce a similar motion at all stations, while a slow slip will produce motions in opposite directions on its different sides. False detections are favored when the number of stations surrounding the event is too low. In our study case of the Mexico subduction zone, the temporal matching of detected slow slips with tremors and LFE occurrences during the MASE observation period corroborates the detections, as they have been observed to occur simultaneously in other subduction zones such as in Cascadia [*Rogers and Dragert*, 2003] and Japan [*Hirose and Obara*, 2005].

4.2. Rate-and-State Asperity Model

In the context of the rate-and-state formalism, velocity-weakening asperities, for which slip can become unstable, can rupture during earthquakes or large SSEs. An initiation of slip evolves into a seismic earthquake or a SSE, mainly depending on its nucleation size [*Liu and Rice*, 2007; *Rubin*, 2008]. A SSE will occur for intermediate nucleation sizes for which the slip can slowly propagate but is too small to induce dynamic instabilities. Numerical models have shown that a velocity-strengthening patch located between two velocity-weakening asperities may act as a barrier to slip propagation if its width is large enough or if it is strongly velocity strengthening [*Kaneko et al.*, 2010]. *Dublanchet et al.* [2013] carried out similar simulations but with clusters of circular velocity-weakening asperities embedded in a velocity-strengthening background. In such a configuration, the slip can propagate throughout a whole cluster, depending on the density of the asperities, a parameter equivalent to the distance between asperities in the two-asperities case. Thus, the product $d(a-b)\sigma_n$, where d is the density of asperities, $(a-b)$ the frictional parameters, and σ_n the effective normal stress, defines both the probability that all asperities break at once and the inter-SSE coupling. In the context of the Mexico subduction zone, $M_w > 7.5$ SSEs that occurred in 2006, 2009–2010, and 2014 take place in areas of high interseismic coupling [*Radiguet et al.*, 2012; *Rousset et al.*, 2016b; *Graham et al.*, 2016]. Of the 28 slow slip events detected in this study, 26 are all located at the edges of the large SSEs, also coincident with average inter-SSE coupling values of ~0.5, while the maximum slip amplitude of large SSEs coincides with an interseismic coupling of ~0.7. We can thus think that the occurrence of these newly detected M_w 6 to 7 slow slip events is a way to progressively destabilize the cluster of asperities by its edges before the initiation of a large SSE on the whole cluster of asperities. The same kind of process seems to occur before some seismic events, preceded by slow slips around the main slip area, such as the Iquique or the Illapel sequences in Chile [*Ruiz et al.*, 2014, 2016]. In other cases, seismic events surround the main aseismic slip [*Villegas-Lanza et al.*, 2015].

4.3. Scaling Laws

Some studies have suggested that different scaling laws govern fast earthquakes and slow earthquakes, fast and slow referring to the velocity slip front. The moment magnitude of fast earthquakes is generally proportional to the cube of their duration, while the moment magnitude of slow earthquakes has been proposed to be proportional to their duration [e.g., *Ide et al.*, 2007]. The main weakness of the estimated scaling law for slow events is that it is constrained by two end-member populations of events with a gap in between. The first population of events is made of tremors and LFEs that last seconds to minutes, while the second population is made up of slow slip recorded by geodetic instruments that last days to months. In the Mexico subduction zone, slow slip events (including those newly detected in this study) cover a large range of magnitudes

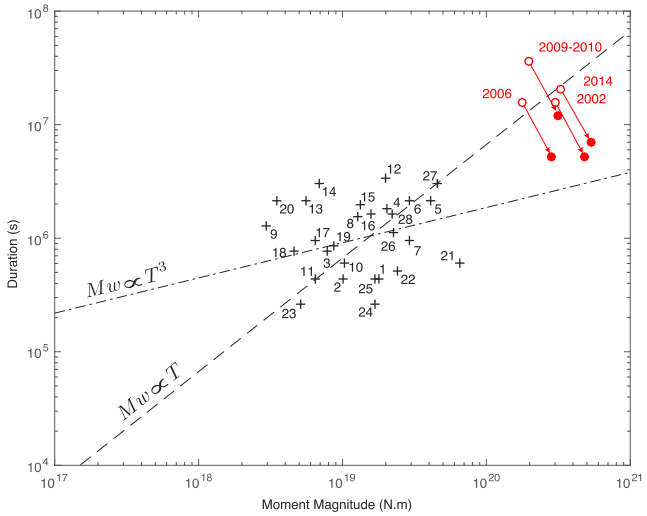

Figure 14. Duration of detected slow slip events as a function of their moment magnitude. The black crosses represent all the detected events of this study. The open red circles indicate the duration and moment magnitude for the 2002, 2006, 2009–2010, and 2014 slow slip events [*Radiguet et al.*, 2012, 2016]. The solid red circles correspond to the duration and moment magnitude of the release periods of large slow slip events, based on *Frank et al.* [2017]. The dashed line is the best fit to the events detected in this study (black crosses), using a linear relation between the log of the duration and the log of the moment magnitude (slow earthquakes scaling law proposed by *Ide et al.* [2007]). The dash-dotted line is the best fit for a linear relation between the log of the moment magnitude and the log of the cube of the duration (slope of the fast earthquakes scaling law).

from M_w 6.3 to M_w 7.6 and might help to constrain the scaling within slow slip events. In Figure 14, we compare the distribution in duration and magnitude of all detected events to the theoretical scaling laws of slow and fast earthquakes. While the error on the duration and magnitudes on the 28 detected events is difficult to estimate, coming from various sources, it is limited to about 10 days for durations and 0.4 for the magnitudes, based on our synthetic tests (see section 2.4). Thus, these 28 events form a cluster of events in the duration-magnitude plot and the slope of the scaling law is constrained by the slope between this cluster and the $M_w > 7.5$ events. Taking into account the durations and magnitudes estimated from the modeling of the long-period GPS measurements [*Radiguet et al.*, 2012; *Graham et al.*, 2016; *Radiguet et al.*, 2016, empty red dots on Figure 14], the scaling seems to be in agreement with a law for which the moment magnitude scales with the duration, as in *Ide et al.* [2007]. However, if we consider the recent findings of *Frank et al.* [2017], based on the short-timescale evolution of the 2006 slow slip, large slow slip events are made of a succession of loading and release periods, leading to reduced durations and increased moment magnitudes. For the 2006 event, the release period corresponds to a third of the total duration and the release displacement at station MEZC is 1.6 times larger than the displacement of the total SSE period. Not having the same analysis for other large SSEs, we might consider similar scaling factors for durations and magnitudes for the other, equivalent size slow slips, as shown in Figure 14 (filled red dots). The linear relation between the events detected in this study (black crosses in Figure 14) and the reestimated durations and magnitudes of large SSEs (filled red dots in Figure 14) would then be closer to a scaling of classical earthquakes, with the moment magnitude proportional to the duration power 1 to 2. Similar powers has been found in numerical models of slow slips with fractal and nonuniform distributions of slip [*Ben-Zion*, 2012]. We also note that the release duration estimated in *Frank et al.* [2017] is likely to be overestimated, because the lower threshold in the estimates of release periods is set by the daily sampling rate of GPS. Shorter durations would lead to scaling even closer to the ones of seismic earthquakes. However, as our detections have been done with GPS data, it is also possible that the detected events include both release and loading periods, which would also reduce the estimated durations and increase the estimated magnitude. It is worth noting that independent observations of low-frequency earthquakes [*Bostock et al.*, 2015] or secondary slip fronts [*Bletery et al.*, 2017] taken individually exhibit different scaling than the one proposed by *Ide et al.* [2007]. It is thus difficult to validate a simple scaling law from the ensemble of slow slip events detected in this study, and more refined studies with higher GPS sampling rates measurements would probably help better constrain the scaling of slow earthquakes.

5. Conclusion

We have developed a geodetic matched filter that allows us to search for slow transient slip events on faults based on a physical model. Correlation functions between template surface displacement time series and GPS time series are computed, carefully weighted, and summed over both GPS horizontal components

and all stations in a network, to enhance the signal-to-noise ratio and detect small events below the noise level. A statistical analysis of synthetic tests, in the context of the Mexico subduction zone, allows us to discuss the accuracy of the method in characterizing the timing, location, duration, and magnitude of slow events. We show that for $M_w > 6$ events, these parameters can be well estimated, although the resolution will depend both on the quality of the time series and the density of the network around a potential slip event. The application to real time series in the area of the Guerrero gap, for the period from 2005 to 2014, allows us to identify 28 SSEs of M_w between 6.3 and 7.2, mainly located downdip of the 2006, 2009–2010, and 2014 large events slip areas, with some small SSEs close to the initiation area of large SSEs. This study thus sheds light on the dynamics of slip on tectonic plates interfaces and on potential interactions between slip events at various scales. With growing networks of GPS around the world, our new approach takes advantage of the redundancy of information over a network and can be applied to longer time periods and in various tectonic contexts.

Acknowledgments
We thank the Geophysics Institute of the National Autonomous University of Mexico (UNAM) for providing us the raw files used to process the GPS time series. These data have recently been made publicly available via the Laboratorio de Geodesia Satelital (LaGeos, contact: ivonne@igeofisica.unam.mx). Part of the GPS data was obtained by the Servicio Sismológico Nacional (SSN, Mexico). Thanks are given to its personnel for station maintenance, data acquisition, and distribution. We appreciate the efforts of Jose Antonio Santiago, Jorge Real, and Enrique Cabral Cano in maintaining the UNAM GPS networks. The GPS time series have been processed at ISTerre using the open source GAMIT/GLOBK softwares, available at http://www-gpsg.mit.edu/~simon/gtgk/. For most of the GPS stations, independently processed time series are also available from the UNAVCO GPS platform (https://www.unavco.org/data/gps-gnss/gps-gnss.html) and the Nevada Geodetic Laboratory (http://geodesy.unr.edu). We are grateful to the LabexOSUG@2020, Investissements d'avenirANR10 LABX56, and the French spatial agency CNES, project TOSCA SSEMEX for having funded the GPS processing. W.B. Frank was supported by NSF grant EAR-PF 1452375. We thank R. Bürgmann for constructive comments. This manuscript has been greatly improved by the reviews made by A. Thomas and an anonymous reviewer.

References

Altamimi, Z., X. Collilieux, and L. Métivier (2011), ITRF2008: An improved solution of the international terrestrial reference frame, *J. Geod.*, *85*(8), 457–473.

Bartlow, N. M., S. Miyazaki, A. M. Bradley, and P. Segall (2011), Space-time correlation of slip and tremor during the 2009 Cascadia slow slip event, *Geophys. Res. Lett.*, *38*, L18309, doi:10.1029/2011GL048714.

Ben-Zion, Y. (2012), Episodic tremor and slip on a frictional interface with critical zero weakening in elastic solid, *Geophys. J. Int.*, *189*(2), 1159–1168.

Bletery, Q., A. M. Thomas, J. C. Hawthorne, R. M. Skarbek, A. W. Rempel, and R. D. Krogstad (2017), Characteristics of secondary slip fronts associated with slow earthquakes in Cascadia, *Earth Planet. Sci. Lett.*, *463*, 212–220.

Bostock, M. G., A. M. Thomas, G. Savard, L. Chuang, and A. M. Rubin (2015), Magnitudes and moment-duration scaling of low-frequency earthquakes beneath Southern Vancouver Island, *J. Geophys. Res. Solid Earth*, *120*, 6329–6350, doi:10.1002/2015JB012195.

Bouchon, M. (1981), A simple method to calculate Green's functions for elastic layered media, *Bull. Seismol. Soc. Am.*, *71*(4), 959–971.

Bouchon, M. (2003), A review of the discrete wavenumber method, *Pure Appl. Geophys.*, *160*(3-4), 445–465.

Brown, J. R., S. G. Prejean, G. C. Beroza, J. S. Gomberg, and P. J. Haeussler (2013), Deep low-frequency earthquakes in tectonic tremor along the Alaska-Aleutian subduction zone, *J. Geophys. Res. Solid Earth*, *118*, 1079–1090, doi:10.1029/2012JB009459.

Caltech (2007), Meso-America subduction experiment, *Caltech Dataset*, doi:10.7909/C3RN35SP.

Cavalié, O., E. Pathier, M. Radiguet, M. Vergnolle, N. Cotte, A. Walpersdorf, V. Kostoglodov, and F. Cotton (2013), Slow slip event in the Mexican subduction zone: Evidence of shallower slip in the Guerrero seismic gap for the 2006 event revealed by the joint inversion of InSAR and GPS data, *Earth Planet. Sci. Lett.*, *367*, 52–60.

Coutant, O., (1989), Programme de simulation numerique AXITRA, Rapport LGIT, Univ. Joseph Fourier, Grenoble, France.

Dragert, H., K. Wang, and T. S. James (2001), A silent slip event on the deeper Cascadia subduction interface, *Science*, *292*(5521), 1525–1528.

Dublanchet, P., P. Bernard, and P. Favreau (2013), Interactions and triggering in a 3-D rate-and-state asperity model, *J. Geophys. Res. Solid Earth*, *118*, 2225–2245, doi:10.1002/jgrb.50187.

Frank, W. B. (2016), Slow slip hidden in the noise: The intermittence of tectonic release, *Geophys. Res. Lett.*, *43*, 10,125–10,133, doi:10.1002/2016GL069537.

Frank, W. B., N. M. Shapiro, V. Kostoglodov, A. L. Husker, M. Campillo, J. S. Payero, and G. A. Prieto (2013), Low-frequency earthquakes in the Mexican Sweet Spot, *Geophys. Res. Lett.*, *40*, 2661–2666, doi:10.1002/grl.50561.

Frank, W. B., N. M. Shapiro, A. L. Husker, V. Kostoglodov, A. Romanenko, and M. Campillo (2014), Using systematically characterized low-frequency earthquakes as a fault probe in Guerrero, Mexico, *J. Geophys. Res. Solid Earth*, *119*, 7686–7700, doi:10.1002/2014JB011457.

Frank, W. B., M. Radiguet, B. Rousset, N. M. Shapiro, A. L. Husker, V. Kostoglodov, N. Cotte, and M. Campillo (2015), Uncovering the geodetic signature of silent slip through repeating earthquakes, *Geophys. Res. Lett.*, *42*, 2774–2779, doi:10.1002/2015GL063685.

Frank, W. B., B. Rousset, C. Lasserre, and M. Campillo (2017), Revealing the cascade of slow transients behind a large slow slip event, *Nat. Geosci.*, doi:arXiv:1711.11528v1.

Gibbons, S. J., and F. Ringdal (2006), The detection of low magnitude seismic events using array-based waveform correlation, *Geophys. J. Int.*, *165*(1), 149–166.

Graham, S., C. DeMets, E. Cabral-Cano, V. Kostoglodov, B. Rousset, A. Walpersdorf, N. Cotte, C. Lasserre, R. McCaffrey, and L. Salazar-Tlaczani (2016), Slow slip history for the Mexico subduction zone: 2005 through 2011, *Pure Appl. Geophys.*, *173*(10-11), 3445–3465.

Hernandez, B., N. M. Shapiro, S. K. Singh, J. F. Pacheco, F. Cotton, M. Campillo, A. Iglesias, V. Cruz, J. M. Gómez, and L. Alcántara (2001), Rupture history of September 30, 1999 intraplate earthquake of Oaxaca, Mexico ($M_W = 7.5$) from inversion of strong-motion data, *Geophys. Res. Lett.*, *28*(2), 363–366.

Herring, T. A., R. W. King, and S. C. McClusky (2006), *Gamit Reference Manual*, GPS Analysis at MIT, release 10, 36, Cambridge, Mass.

Hirose, H., and K. Obara (2005), Repeating short- and long-term slow slip events with deep tremor activity around the Bungo channel region, southwest Japan, *Earth Planets Space*, *57*(10), 961–972.

Husker, A. L., V. Kostoglodov, V. M. Cruz-Atienza, D. Legrand, N. M. Shapiro, J. S. Payero, M. Campillo, and E. Huesca-Pérez (2012), Temporal variations of non-volcanic tremor (NVT) locations in the Mexican subduction zone: Finding the NVT sweet spot, *Geochem. Geophys. Geosyst.*, *13*, Q03011, doi:10.1029/2011GC003916.

Ide, S., G. C. Beroza, D. R. Shelly, and T. Uchide (2007), A scaling law for slow earthquakes, *Nature*, *447*(7140), 76–79.

Ji, K. H., and T. A. Herring (2013), A method for detecting transient signals in GPS position time-series: Smoothing and principal component analysis, *Geophys. J. Int.*, *193*(1), 171–186.

Jolivet, R., C. Lasserre, M.-P. Doin, G. Peltzer, J.-P. Avouac, J. Sun, and R. Dailu (2013), Spatio-temporal evolution of aseismic slip along the Haiyuan fault, China: Implications for fault frictional properties, *Earth Planet. Sci. Lett.*, *377*, 23–33.

Kaneko, Y., J.-P. Avouac, and N. Lapusta (2010), Towards inferring earthquake patterns from geodetic observations of interseismic coupling, *Nat. Geosci.*, *3*(5), 363–369.

Kim, Y., R. W. Clayton, and J. M. Jackson (2010), Geometry and seismic properties of the subducting cocos plate in central Mexico, *J. Geophys. Res.*, *115*, B06310, doi:10.1029/2009JB006942.

Kostoglodov, V., A. Husker, N. M. Shapiro, J. S. Payero, M. Campillo, N. Cotte, and R. Clayton (2010), The 2006 slow slip event and nonvolcanic tremor in the Mexican subduction zone, *Geophys. Res. Lett.*, *37*, L24301, doi:10.1029/2010GL045424.

Linde, A. T., M. T. Gladwint, M. J. S. Johnston, R. L. Gwythert, and R. G. Bilham (1996), A slow earthquake sequence on the San Andreas fault, *Nature*, *383*, 65–68.

Liu, Y., and J. R. Rice (2007), Spontaneous and triggered aseismic deformation transients in a subduction fault model, *J. Geophys. Res.*, *112*, B09404, doi:10.1029/2007JB004930.

McGuire, J. J., and P. Segall (2003), Imaging of aseismic fault slip transients recorded by dense geodetic networks, *Geophys. J. Int.*, *155*(3), 778–788.

Miyazaki, S., J. J. McGuire, and P. Segall (2003), A transient subduction zone slip episode in southwest Japan observed by the nationwide GPS array, *J. Geophys. Res.*, *108*(B2), 2087, doi:10.1029/2001JB000456.

Nishimura, T. (2014), Short-term slow slip events along the Ryukyu Trench, southwestern Japan, observed by continuous GNSS, *Prog. Earth Planet. Sci.*, *1*(1), 22.

Nishimura, T., T. Matsuzawa, and K. Obara (2013), Detection of short-term slow slip events along the Nankai Trough, southwest Japan, using GNSS data, *J. Geophys. Res. Solid Earth*, *118*, 3112–3125, doi:10.1002/jgrb.50222.

Obara, K., and A. Kato (2016), Connecting slow earthquakes to huge earthquakes, *Science*, *353*(6296), 253–257.

Ohtani, R., J. J. McGuire, and P. Segall (2010), Network strain filter: A new tool for monitoring and detecting transient deformation signals in GPS arrays, *J. Geophys. Res.*, *115*, B12418, doi:10.1029/2010JB007442.

Radiguet, M., F. Cotton, M. Vergnolle, M. Campillo, A. Walpersdorf, N. Cotte, and V. Kostoglodov (2012), Slow slip events and strain accumulation in the Guerrero gap, Mexico, *J. Geophys. Res.*, *117*, B04305, doi:10.1029/2011JB008801.

Radiguet, M., H. Perfettini, N. Cotte, A. Gualandi, B. Valette, V. Kostoglodov, T. Lhomme, A. Walpersdorf, EC. Cano, and M. Campillo (2016), Triggering of the 2014 M_w7.3 Papanoa earthquake by a slow slip event in Guerrero, Mexico, *Nat. Geosci.*, *9*(11), 829–833.

Riel, B., M. Simons, P. Agram, and Z. Zhan (2014), Detecting transient signals in geodetic time series using sparse estimation techniques, *J. Geophys. Res. Solid Earth*, *119*, 5140–5160, doi:10.1002/2014JB011077.

Rogers, G., and H. Dragert (2003), Episodic tremor and slip on the Cascadia subduction zone: The chatter of silent slip, *Science*, *300*(5627), 1942–1943.

Rousset, B., R. Jolivet, M. Simons, C. Lasserre, B. Riel, P. Milillo, Z. Çakir, and F. Renard (2016a), An aseismic slip transient on the North Anatolian Fault, *Geophys. Res. Lett.*, *43*, 3254–3262, doi:10.1002/2016GL068250.

Rousset, B., et al. (2016b), Lateral variations of interplate coupling along the Mexican subduction interface: Relationships with long-term morphology and fault zone mechanical properties, *Pure Appl. Geophys.*, *173*(10–11), 3467–3486, doi:10.1007/s00024-015-1215-6.

Rubin, A. M. (2008), Episodic slow slip events and rate-and-state friction, *J. Geophys. Res.*, *113*, B11414, doi:10.1029/2008JB005642.

Ruiz, S., M. Metois, A. Fuenzalida, J. Ruiz, F. Leyton, R. Grandin, C. Vigny, R. Madariaga, and J. Campos (2014), Intense foreshocks and a slow slip event preceded the 2014 Iquique M_w 8.1 earthquake, *Science*, *345*(6201), 1165–1169.

Ruiz, S., et al. (2016), The seismic sequence of the 16 September 2015 M_w 8.3 Illapel, Chile, earthquake, *Seismol. Res. Lett.*, *87*(4), 1.

Segall, P., and M. Matthews (1997), Time dependent inversion of geodetic data, *J. Geophys. Res.*, *102*, 22–391.

Shirzaei, M., and R. Bürgmann (2013), Time-dependent model of creep on the Hayward fault from joint inversion of 18 years of InSAR and surface creep data, *J. Geophys. Res. Solid Earth*, *118*, 1733–1746, doi:10.1002/jgrb.50149.

Vergnolle, M., A. Walpersdorf, V. Kostoglodov, P. Tregoning, J. A. Santiago, N. Cotte, and S. I. Franco (2010), Slow slip events in Mexico revised from the processing of 11 year GPS observations, *J. Geophys. Res.*, *115*, B08403, doi:10.1029/2009JB006852.

Villegas-Lanza, J. C., J.-M. Nocquet, F. Rolandone, M. Vallée, H. Tavera, F. Bondoux, T. Tran, X. Martin, and M. Chlieh (2015), A mixed seismic-aseismic stress release episode in the Andean subduction zone, *Nat. Geosci.*, *9*(2), 150.

Walpersdorf, A., N. Cotte, V. Kostoglodov, M. Vergnolle, M. Radiguet, J. A. Santiago, and M. Campillo (2011), Two successive slow slip events evidenced in 2009–2010 by a dense GPS network in Guerrero, Mexico, *Geophys. Res. Lett.*, *38*, L15307, doi:10.1029/2011GL048124.

Walwer, D., E. Calais, and M. Ghil (2016), Data-adaptive detection of transient deformation in geodetic networks, *J. Geophys. Res. Solid Earth*, *121*, 2129–2152, doi:10.1002/2015JB012424.

Wei, M., D. Sandwell, and Y. Fialko (2009), A silent M_w 4.7 slip event of October 2006 on the Superstition Hills fault, Southern California, *J. Geophys. Res.*, *114*, B07402, doi:10.1029/2008JB006135.

Williams, S. D. P., Y. Bock, P. Fang, P. Jamason, R. M. Nikolaidis, L. Prawirodirdjo, M. Miller, and D. J. Johnson (2004), Error analysis of continuous GPS position time series, *J. Geophys. Res.*, *109*, B03412, doi:10.1029/2003JB002741.